Can the data assimilation of CO from MOPITT or IASI constrain high-latitude wildfire emissions? A Case Study of the 2017 Canadian Wildfires

Erik Lutsch[1], Debra Wunch[1], Dylan B.A. Jones[1], Cathy Clerbaux[2], James W. Hannigan[3], Tai-long He[1], Ivan Ortega[3], Sébastien Roche[1,a], Kimberly Strong[1], Helen Worden[3]

[1]Department of Physics, University of Toronto, Toronto, Canada
[2]LATMOS/IPSL, Sorbonne Université, UVSQ, CNRS, Paris, France
[3]Atmospheric Chemistry Observations & Modeling, National Center for Atmospheric Research, Boulder, CO, USA
[a]now at: School of Engineering and Applied Sciences, Harvard University, Cambridge, MA, USA

Key Points:

- MOPITT and IASI CO measurements provide consistent posteriori emissions globally with regional differences for the 2017 Canadian wildfires.
- The 3-day global coverage of MOPITT limits its ability to optimize emissions, while the daily coverage of IASI yields a modest improvement.
- Temporal coverage of IASI most strongly influenced the posteriori estimates, while vertical sensitivity had a minor contribution.

Corresponding author: Erik Lutsch, elutsch@physics.utoronto.ca

Abstract

In this study, we examine the ability of the data assimilation of global satellite-based carbon monoxide (CO) observations to constrain high-latitude boreal wildfire emissions. We compare the optimized emissions from inversions using CO measurements from the Measurement of Pollution in the Troposphere (MOPITT) and Infrared Atmospheric Sounding Interferometer (IASI). We found that both inversions yield generally consistent posterior CO emissions globally; however, distinct differences are observed for the episodic 2017 Canadian wildfires. The 3-day global coverage of MOPITT limits its ability to accurately optimize emissions, while the daily global coverage of IASI provides a moderate improvement despite its lower surface sensitivity. Through a series of observing system simulation experiments (OSSEs), we show that the temporal coverage of IASI most strongly influenced the posterior estimates, while the differences in vertical sensitivities of MOPITT and IASI have a minor contribution.

1 Introduction

The Arctic is a major receptor for pollution from mid-latitude regions (Stohl, 2006; Law & Stohl, 2007; Shindell et al., 2008). Through the emissions of greenhouse gases, trace gases and particulate species, high-latitude boreal wildfires have significant impacts on Arctic air quality and climate (Amiro et al., 2009; Warneke et al., 2009). Wildfires are also a major driver of the boreal net ecosystem carbon balance. Climate warming and drying has led to more severe and frequent forest fires, with this trend expected to increase with future climate change (Kasischke & Turetsky, 2006; de Groot et al., 2013). Increasing wildfire emissions in the future may reverse the carbon balance of the boreal ecosystem from a net sink to net source (Bond-Lamberty et al., 2007), resulting in a positive climate feedback (Li et al., 2017). Carbon monoxide (CO), a product of incomplete combustion, is considered an ideal tracer of biomass burning as it is emitted in a large abundance across all wildfire regimes globally (e.g. Andreae (2019)). Since CO is co-emitted with greenhouse gases, reactive trace gases, and particulate species, observations of CO can be utilized to improve our understanding of factors influencing boreal fire emissions and their impact on atmospheric composition and chemistry.

Global chemical transport models (CTMs) are used to simulate the impact of emissions, transport and chemistry on the atmospheric abundance of a large number of gas phase and particulate species. Global CTMs, in all cases, rely on a number of param-

eterizations of the emissions, chemistry and transport within the model, in order to simulate atmospheric processes at finite resolution, both in space and time. All CTMs suffer errors as a result of the finite chemical and transport operators (Philip et al., 2016), while transport errors are inherent in the meteorological fields reanalyses that are used to drive the models (Yu et al., 2018). Simulations of biomass burning emissions and their transport are also highly uncertain. Most biomass burning emissions inventories, including the commonly used Fire Inventory from NCAR (FINN; Wiedinmyer et al. (2011)), the Quick Fire Emission Database (QFED; Koster et al. (2015)), the Global Fire Emission Database (GFED; van der Werf et al. (2017)) and the Global Fire Assimilation System (GFAS; Kaiser et al. (2012)), are all bottom-up inventories, in which satellite observations of burned areas, burned fraction, fire-radiative power (FRP), and vegetation type are used to estimate the total dry matter burned. The mass of dry matter burned is scaled by the emission factor (EF, e.g. Andreae and Merlet (2001); Akagi et al. (2011); Andreae (2019)) for a particular species to yield the total mass of the species emitted. Each quantity used in the estimation of these emissions is subject to its own uncertainty, leading to errors in the calculated total emissions of biomass burning.

In the case of an episodic wildfire plume, global CTMs generally do not take into account direct injection of emissions into the free troposphere which may often occur (Val Martin et al., 2010, 2018). Injection of emissions into the free troposphere can result in different transport pathways of the plume compared to those from near-surface emissions. Accounting for this may be particularly important for more accurately capturing the long-range transport of a plume. Long-range transport errors are exacerbated by the numerical diffusion in coarse-resolution CTMs, further reducing the accuracy of simulations of the transport of episodic wildfire plumes (Rastigejev et al., 2010; Eastham & Jacob, 2017).

In contrast to bottom-up biomass burning emission inventories, satellite-based observations can provide top-down estimates on wildfire emissions. Currently, several satellite-based instruments routinely measure CO globally, including the Measurements of Pollution of the Troposphere (MOPITT) (Deeter, 2003), Atmospheric Infrared Sounder (AIRS) (Aumann et al., 2003), Atmospheric Chemistry Experiment Fourier Transform Spectrometer (ACE-FTS) (Clerbaux et al., 2008), Cross-track Infrared Spectrometer (CrIS) (Fu et al., 2016), Infrared Atmosphere Sounding Interferometer (IASI) (Clerbaux et al., 2009), and the Tropospheric Monitoring Instrument (TROPOMI) (Landgraf et al., 2016). Each

of these instruments provides global observations of CO with varying temporal and horizontal resolution, and vertical sensitivity.

To quantify global emissions of CO, including wildfire sources, these space-based measurements may be used in a data assimilation approach with global CTMs. Several studies have implemented global satellite observations of CO from MOPITT (e.g. Arellano (2004); Heald et al. (2004); Fortems-Cheiney et al. (2011); Jiang et al. (2011, 2015); Yin et al. (2015); Jiang et al. (2017); X. Zhang et al. (2020)) and IASI (e.g. Muller et al. (2018); Zheng et al. (2019)) to quantify and refine global CO source emission inventories. However, few studies have focused on the high-latitude boreal wildfires. Pfister et al. (2005) performed a case study using the using regional-scale data assimilation of MOPITT CO to quantify boreal wildfire emissions of CO from the 2004 Alaskan wildfire season. Gonzi et al. (2011) used MOPITT CO observations to identify seasonal trends of global wildfire sources. However, due the episodic nature of high-latitude wildfires and the limited observations in high-latitude regions, the ability for the data assimilation of global CO measurements to accurately constrain these emissions remains uncertain, particularly with respect to the temporal coverage and vertical sensitivity of the measurements.

The data assimilation of MOPITT and IASI to optimize the global CO state have been performed in past studies (e.g. Barré, Gaubert, et al. (2015); Barré, Edwards, et al. (2015); Inness et al. (2013, 2015)). Inness et al. (2013) examined the Monitoring Atmospheric Composition and Climate (MACC) reanalysis and found that the assimilation of IASI CO resulted in a greater low-bias of CO in the Northern high-latitudes as opposed to the assimilation of MOPITT CO, through comparison to independent measurement datasets. Comparisons of the data assimilation of MOPITT and IASI CO were examined by Barré, Gaubert, et al. (2015) and concluded that both MOPITT and IASI constrain the CO state close to the main anthropogenic, biogenic and biomass burning sources, while IASI provided improved constraints on far-away CO sources. Furthermore, IASI provided better constraints on the global CO field, while MOPITT provided stronger constraints on near-surface CO in the main source regions as compared to independent measurements. However, comparison of the ability of the data assimilation of MOPITT or IASI to optimize emission sources has not yet been studied.

In this study, we assess and compare the ability of satellite observations of CO to optimize high-latitude boreal wildfire emissions using measurements of CO from the MO-

PITT and IASI instruments in order to distinguish the contribution of the temporal coverage and vertical sensitivity of the measurements. We examine a case study of the 2017 Canadian wildfires, which contained two separate wildfire events in British Columbia (BC) and the Northwest Territories (NWT) of Canada in August 2017 (Lutsch et al., 2019). Emissions for these wildfires resulted in large-scale perturbations to atmospheric CO (e.g. Lutsch et al. (2019, 2020)) and aerosols (e.g., Khaykin et al. (2018); Peterson et al. (2018); Ranjbar et al. (2019)) throughout the Northern Hemisphere. Due to the large-scale impact of these wildfires, these events provide an ideal case to examine the ability of our data assimilation system to precisely locate and optimize their emissions.

The structure of this paper is as follows. Section 2.1 presents the satellite and ground-based measurements used in this study. Section 2.2 describes the GEOS-Chem adjoint model and its configuration as implemented for this study. The global and regional posterior emission estimates obtained from MOPITT and IASI are presented and discussed in Section 3.1. Sections 3.2 and 3.3 examine the regional analysis of the high-latitude boreal wildfires and the 2017 Canadian wildfires, respectively. The inversions are evaluated using high-latitude ground-based measurements in Section 3.4. To examine the impact of measurement temporal coverage and vertical sensitivity, a series of observing system simulation experiments (OSSEs) were performed and the results are highlighted and interpreted in Section 3.5. Lastly, a summary of the study and suggestions for future studies are provided in Section 4

2 Methods

2.1 Measurements and Instruments

2.1.1 MOPITT

The Measurement of Pollution in the Troposphere (MOPITT) instrument was launched in December 1999 aboard the NASA Terra satellite. Full details of the MOPITT instrument are provided by Drummond et al. (2010) and are presented briefly here. MOPITT is a nadir-viewing gas correlation radiometer. Since August 2001, measurements of CO are made using two thermal-infrared (TIR) bands (channels no. 5 and no. 7; 4.617±0.055 μm) and one near-infrared (NIR) band (channel no. 6; 2.334±0.011 μm). A linear detector array allows MOPITT to record simultaneous measurements at four different sounding locations, each with field-of-view of approximately 22 × 22 km^2. The Terra satel-

lite is in a daytime-descending, Sun-synchronous orbit at an altitude of approximately 700 km, with an equator crossing time of 10:30 local time. Terra makes approximately 14-15 orbits per day and the instrument achieves near-global coverage every 3 to 4 days.

There are three retrieval products of CO from MOPITT: the TIR-only (T), NIR-only (N) and the joint TIR-NIR retrieval (J). We use total column measurements from the TIR-NIR MOPITT v8 (v8J; (Deeter et al., 2019)) retrieval product because it provides the most vertical information. MOPITT retrievals of CO are performed using an iterative optimal estimation algorithm (OEM; Rodgers (2000)) utilizing MOPITT calibrated radiances and a priori knowledge of CO variability (Deeter et al., 2014, 2017; Lamarque et al., 2012). Volume mixing ratio (VMR) retrievals are performed in log-space to retrieve log(VMR) on a 10-layer vertical retrieval grid from the surface to 100 hPa. Total columns of CO are calculated directly from the retrieved CO VMR profile. A priori CO profiles are derived from a model climatology which varies seasonally and geographically; the a priori climatology was introduced for processing MOPITT version 7 products (Deeter et al., 2017). The a priori value is from climatological output from the Community Atmosphere Model with Chemistry (CAM-chem; Lamarque et al. (2012)) and is described by Deeter et al. (2014). The a priori covariance matrix is described by Deeter et al. (2010).

In addition to validation with in situ aircraft CO measurements (Deeter et al., 2019), MOPITT CO products have been validated against ground-based Fourier-transform infrared (FTIR) measurements. Buchholz et al. (2017) performed a comparison of MOPITT v6 CO products against 14 global ground-based mid-infrared FTIR measurement sites of the Network for Detection of Atmospheric Composition Change (NDACC). Biases were found to vary between MOPITT CO products with mean biases across all sites of 2.4% for TIR-only, 5.1% for joint TIR-NIR, and 6.5% for NIR-only. The bias was found not to depend on latitude but rather on proximity to CO sources, with larger biases near local sources. MOPITT v8 has been validated against near-infrared FTIR measurements of the Total Carbon Column Observing Network (TCCON) by Hedelius et al. (2019). A high-bias of the MOPITT v8 joint TIR-NIR product against the TCCON FTIR measurements was observed, which generally varied between 6-8% across 31 measurement sites.

2.1.2 IASI

We use CO total column abundances retrieved from observations by the IASI instrument on board the Metop-A satellite. Full details of the IASI instrument are provided by Clerbaux et al. (2009). The satellite has a Sun-synchronous polar-orbit providing twice daily global coverage at 9:30 local time and 21:30 local time overpasses. To maintain consistency with MOPITT, we only use IASI observations from the morning overpass. IASI is a Fourier-transform spectrometer with a spectral range of 15.5 to 3.62 μm (645 to 2760 cm^{-1}). Raw measurements from IASI are interferograms which are processed and transformed into radiometrically calibrated spectra. The maximum optical path difference is $\pm$2 cm which leads to 0.5 cm^{-1} full width at half-maximum apodized spectral resolution. Over a swath width of $\sim$2200 km, a total of 120 views are collected for 30 arrays of four individual elliptical pixels. Each pixel has a 12 km diameter at nadir which increases at the larger viewing angles.

We used the most recent CO data product: FORLI v20140922 (`https://iasi.aeris-data.fr/co/`) described by Hurtmans et al. (2012). Retrievals of CO take advantage of absorption in the fundamental 1-0 CO rotation-vibration band centered around 4.7 μm. CO is retrieved at each location with vertical sensitivity that is dependent on the absorption of interfering species, vertical concentration profile of the species, local surface temperature and emissivity, the vertical temperature profile, and the measurement noise and spectral resolution. For thermal-infrared measurements of CO, the vertical information content is mainly attributed to the mid-troposphere.

The FORLI-CO product (Hurtmans et al., 2012) was used in this study and is based on OEM to retrieve CO profiles on a 19-layer retrieval grid. The a priori information and error covariance are constructed from a database of observations from MOZAIC IAGOS (Measurement of Ozone and Water Vapor by Airbus In-service Aircraft, In-service Aircraft for a Global Observing System flights) and ACE-FTS (Clerbaux et al., 2008). Prior information is complemented with the global model LMDz-INCA (Laboratoire de Météorologie Dynamique-Interaction with Chemistry and Aerosols) to account for both polluted and ambient conditions (Turquety et al., 2009).

The FORLI-CO product has been validated against ground-based FTIR measurements of NDACC by Kerzenmacher et al. (2012). Mean biases ranged from -4.5% at the Southern Hemisphere site of Wollongong, Australia to a maximum of 10.8% at Bremen,

Germany. Comparisons to measurements obtained on the MOZIAC flights showed biases of less than 13% (De Wachter et al., 2012).

2.1.3 Ground-based Measurements

FTIR mid-infrared measurements are provided by the Network for Detection of Atmospheric Composition Change (NDACC, De Mazière et al. (2018), `www.ndacc.org`). NDACC FTIR instruments record solar-absorption spectra during daylight hours and clear-sky conditions. Measurements are generally made at a spectral resolution of 0.0035 cm^{-1}, with a frequency of ∼20 mins. Vertical mixing ratio profiles and integrated column amounts are retrieved using OEM.

Ancillary measurements for the validation of the inversion results are provided by the Total Carbon Column Observing Network (TCCON; Wunch et al. (2011)), which is a global network of FTIR instruments. Solar absorption spectra recorded in the shortwave infrared with a spectral resolution of 0.02 cm^{-1} are used to perform a profile scaling retrieval to produce total columns of CO. CO is measured as a standard species of TCCON, with a frequency of ∼2-3 mins during daylight hours and clear-sky conditions.

In this study, we have selected two high-Arctic FTIR measurement sites: Eureka (80.05°N, 86.42°W), Canada and Thule (76.53°N, 68.74°W), Greenland. Measurements at both sites were found to be fire-affected during August 2017 as described in detail by Lutsch et al. (2019). The Eureka instrument is affiliated with both the TCCON (Strong et al., 2019) and NDACC networks, contributing measurements to both by measuring in alternating NIR and mid-infrared modes, respectively. The Thule instrument contributes measurements to the NDACC network only.

2.2 The GEOS-Chem Model

The GEOS-Chem CTM is implemented in this study. We use version 35j of the GEOS-Chem adjoint, which is based on the forward-model of GEOS-Chem version 8-02-01. The model is driven with assimilated meteorological fields from the Goddard Earth Observing System version 5.11.0 (GEOS-FP) from the NASA Global Model and Assimilation Office (GMAO). Model simulations were performed at a horizontal resolution of 4°×5° with 47 vertical levels. The model is run using the CO-only mode of GEOS-Chem. This CO-only simulation uses prescribed OH concentrations and we have chosen to use monthly

OH fields provided from TransCom (Patra et al., 2011) following Lutsch et al. (2020), which are based on the experimentally derived OH concentrations of Spivakovsky et al. (2000).

The simulations used the global anthropogenic emission inventory from EDGAR 3.2FT2000 (Olivier & Berdowski, 2001), but this has been selectively substituted by the following regional emission inventories: the US Environmental Protection Agency (EPA) National Emission Inventory (NEI) for 2008 in North America (Olivier & Berdowski, 2001), the Criteria Air Contaminants (CAC) inventory for Canada, the Big Bend Regional Aerosol and Visibility Observational (BRAVO) Study Emissions Inventory for Mexico (Kuhns et al., 2005), the Cooperative Program for Monitoring and Evaluation of the Long-range Transmission of Air Pollutants in Europe (EMEP) inventory for Europe in 2000 and the INTEX-B Asia emissions inventory for 2006 (Q. Zhang et al., 2009). Biomass burning emissions are provided by the Global Fire Assimilation System (GFASv1.2; Kaiser et al. (2012)), which are derived from assimilation of FRP observations of the Moderate Resolution Imaging Spectroradiometer (MODIS) on the Aqua and Terra satellites. GFAS provides global emissions for open fires at a native resolution of $0.1^\circ \times 0.1^\circ$ which have been re-gridded to the $4^\circ \times 5^\circ$ GEOS-Chem horizontal resolution grid. Additional CO sources come from the oxidation of methane and biogenic non-methane volatile organic compounds (NMVOCs) as described in previous studies (Jiang et al., 2017). The biogenic emissions are simulated using the Model of Emissions of Gases and Aerosols from Nature, version 2.0 (MEGANv2.0; Guenther et al. (2006)).

2.2.1 4D-Var Data Assimilation

The GEOS-Chem adjoint provides the ability to optimize emission inventories by assimilating measurements of CO. Emissions are optimized by applying spatially- and time-varying corrective scaling factors to reduce the measurement-model mismatch. Sources of CO are constrained using the 4D-Var data assimilation scheme of GEOS-Chem. The intent of the approach is to minimize the cost function:

$$J(\mathbf{x}) = \sum_{i=1}^{N} \left[\mathbf{F}(\mathbf{x}) - \mathbf{z_i}\right]^T \mathbf{S}_\sigma^{-1} \left[\mathbf{F}(\mathbf{x}) - \mathbf{z_i}\right] + \left[\mathbf{x} - \mathbf{x_a}\right]^T \mathbf{S_a}^{-1} \left[\mathbf{x} - \mathbf{x_a}\right], \tag{1}$$

where $\mathbf{x}$ is the state vector of CO emissions, $\mathbf{x_a}$ is the a priori state vector, $\mathbf{F}(\mathbf{x})$ is the observation operator and $\mathbf{z_i}$ is a given CO measurement. The number of measurements

during the assimilation period is denoted by N. The temporal resolution of the forward model is 1 hr, and therefore the high-resolution CO measurements are temporally averaged to 1 hr and spatially averaged onto the $4^\circ \times 5^\circ$ horizontal grid.

We assume a uniform observation error covariance ($\mathbf{S}_\sigma$) of 20% without spatial correlation for both the MOPITT and IASI assimilation following previous studies (Jiang et al., 2011, 2017). Measurement errors for IASI CO observations typically range from 5-15%. However, a 20% observation error covariance was selected to account for the possibility of greater measurement uncertainties (>15%) in high-latitude regions, and to maintain consistency with the MOPITT assimilation. The a priori covariances are independent of the observations and therefore, the same values were applied to the MOPITT and IASI assimilations. The combustion sources of CO (fossil fuels, biofuels and biomass burning) are combined with the oxidation source from VOCs, assuming a uniform 50% a priori error. The CO source from the oxidation of CH_4 is optimized separately as a globally aggregated source assuming a 25% a priori error.

2.2.2 Assimilation Configuration

Biases in the initial condition for the state of CO can adversely affect the optimized emissions and it is therefore essential to first mitigate these biases before optimizing CO emissions. Due to the differences in the a priori profiles, vertical sensitivity and sampling frequencies leading to differences in the MOPITT and IASI CO measurements, it is necessary to generate separate initial conditions that are unique to each instrument. Initial conditions were generated by assimilating MOPITT or IASI measurements to optimize the CO distribution using the weak-constraint 4D-Var assimilation scheme (Stanevich et al., 2021). Further details of the weak-constraint 4D-Var assimilation scheme are described in Appendix A.

The emissions optimization with the 4D-Var assimilation scheme is performed as follows. The optimized state for 1 June 2017 obtained from the weak-constraint 4D-Var assimilation is used as the initial condition. A 4-month assimilation window was selected (1 June - 1 October 2017). The first month (June) is treated as a spin-up period and the last month (September) is considered as a spin-down period. The spin-down period provides additional observations to constrain emissions in the previous months. The months of July and August are the analysis period corresponding to the peak months of the bo-

real wildfire season. In this emission optimization, the optimized emission estimates are returned as monthly emission scale factors.

For both MOPITT and IASI assimilations, the observations are treated in a super-observations scheme as described by X. Zhang et al. (2019), which reduces the representativeness error associated with the variability of CO measurements within each model grid-box (Miyazaki et al., 2012). For each hour of simulation, observations are binned onto the GEOS-Chem horizontal grid. The model VMR and partial column profiles, for MOPITT and IASI respectively, are transformed following Rodgers and Connor (2003) by the instrument averaging kernel and a priori profiles to yield a smoothed model total column as described in Appendix B. For both MOPITT and IASI observations, we have selected a uniform observation error covariance ($\mathbf{S}_\epsilon$) of 20% of the total column of each measurement as stated in Section 2.2.1 to account for representativeness errors and the influence of random transport errors in the model.

The CO observations only provide constraints on the total amount of CO emitted in a given region and therefore there is insufficient information in the inversion to distinguish between individual source types. As such, combustion sources (i.e., fossil fuel, biofuel, and biomass burning) are aggregated with the CO source from the oxidation of biogenic non-methane NMVOCs as a single source term. The inversions provide a constraint on the CO source in each grid box. The CO source from the oxidation of CH_4 is treated as a single global source.

3 Results & Discussion

3.1 Global Optimized CO Emission Estimates

The total a posteriori CO emissions for July-August 2017 obtained from the MOPITT and IASI inversions are tabulated in Table 1 for the source regions of Figure 1, and are shown in Figure 2. The a posteriori emissions are generally consistent across all regions between the two inversions. The North American anthropogenic CO a posteriori values are 10.3 Tg and 10.9 Tg, for MOPITT and IASI, respectively, which are not significantly different from the a priori of 11.0 Tg. Biomass burning emissions of boreal North America (BONA) are a considerable nearby source with an a priori of 20.0 Tg. MOPITT and IASI a posteriori emissions are 20.2 Tg and 17.1 Tg, respectively. Similarly, European a posteriori emissions are near identical for the MOPITT and IASI in-

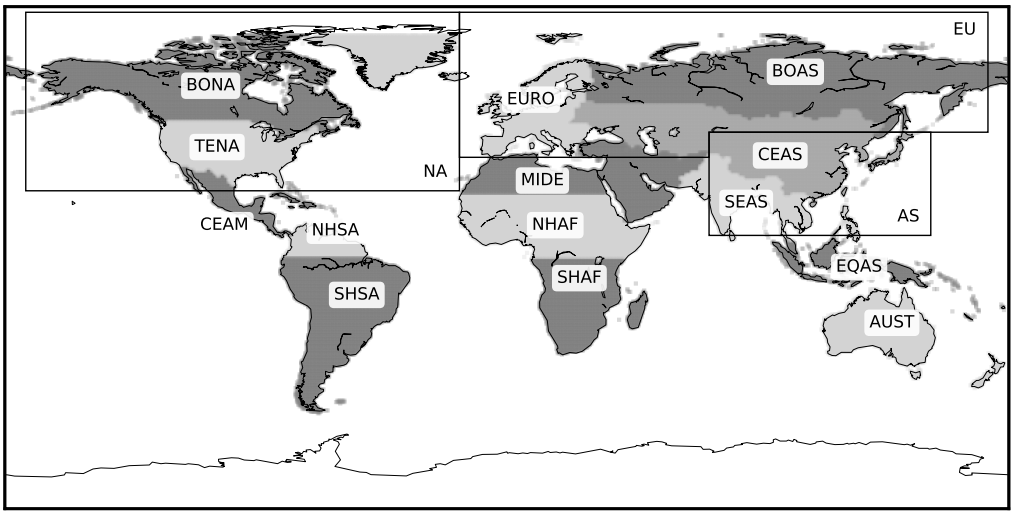

Figure 1. Source regions for biomass burning (shaded), and anthropogenic sources (black rectangles) used for the regional analysis as summarized in Table 1.

versions (10.5 Tg and 10.4 Tg, respectively), which is slightly greater than the a priori of 9.6 Tg. Boreal Asian (BOAS) wildfire emission estimates show more notable differences, with a posteriori emissions of 17.2 Tg and 14.2 Tg for MOPITT and IASI, respectively, compared to an a priori of 17.9 Tg. Small differences are observed between the MOPITT and IASI a posteriori estimates for Temperate North America (TENA) and Central Asia (CEAS) which are a minor contribution to Northern Hemisphere biomass burning sources, while Europe (EURO) are identical. The rest of the world (ROW; sum of all other regions) biomass burning a posteriori estimates are consistent between the two inversions with a difference of ∼4%.

Asian anthropogenic a posteriori emissions are both lower than the a priori (48.2 Tg) for the MOPITT (33.2 Tg) and IASI (37.7 Tg) inversions. This result is consistent with past studies illustrating a decreasing trend of CO emissions in this region (e.g., Jiang et al. (2017)). Elsewhere (ROW), a posteriori anthropogenic emissions are greater than the a priori in both inversions, which is indicative of the increasing trend of CO emissions in developing countries. The differences in the MOPITT and IASI a posteriori estimates for the sources from ROW biomass burning, and CH_4 and NMVOCs oxidation sources are not significantly different.

Table 1. Total a priori and a posteriori CO emissions from the MOPITT and IASI inversions for July - August 2017.

Type	Name	Description	a priori [Tg]	MOPITT [Tg]	IASI [Tg]
Anthro.	NA	North America	11.0	10.3	10.9
	EU	Europe	9.6	10.5	10.4
	AS	Asia	48.2	33.2	37.7
	ROW	Rest of World	16.6	19.0	23.1
Biomass	BONA	Boreal North America	20.0	20.2	17.1
	TENA	Temperate North America	1.9	2.0	2.6
	BOAS	Boreal Asia	17.9	17.2	14.2
	EURO	Europe	0.5	0.6	0.6
	CEAS	Central Asia	4.7	4.7	5.2
	ROW	Rest of the World	41.1	65.8	68.6
Other	CH_4	Methane Oxidation	178.4	179.9	182.6
	NMVOC	NMVOC Oxidation	134.7	141.7	147.7

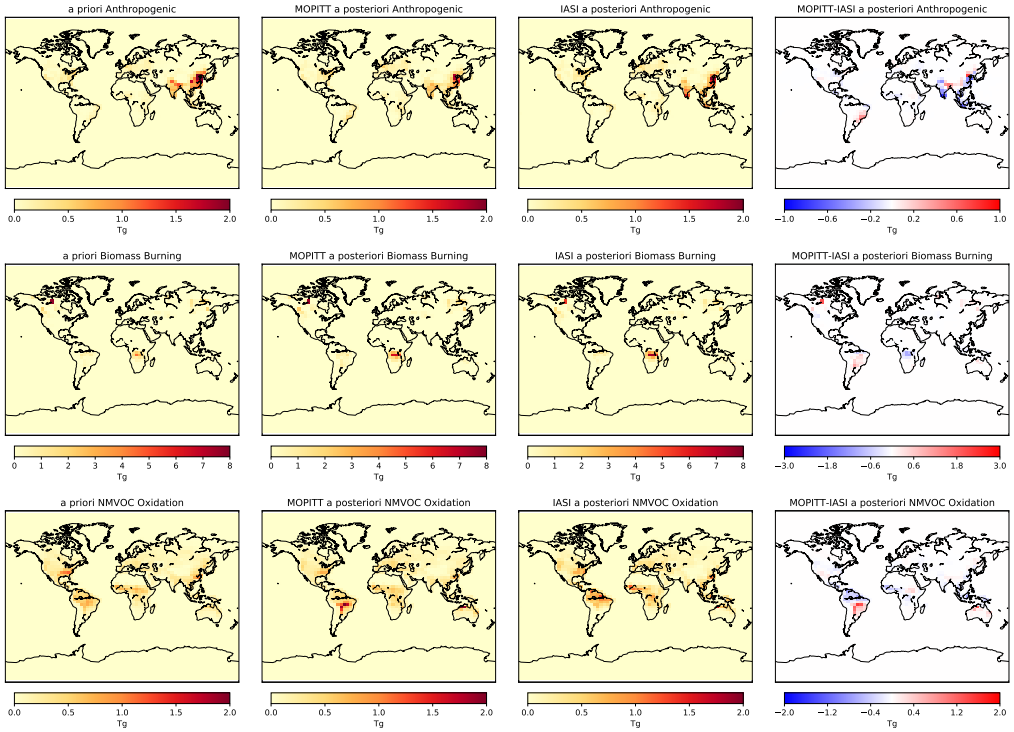

Figure 2. MOPITT and IASI inversion a priori and a posteriori CO emissions for July-August 2017 for anthropogenic, biomass burning and NMVOC oxidation sources. Differences between the a posteriori estimates of the MOPITT and IASI inversion are also shown.

3.2 Regional Analysis of High-latitude Wildfires

In this section, we present the results of the MOPITT and IASI emission inversions for July - August 2017 focusing on the high-latitude boreal wildfire regions of BONA and BOAS. The results are tabulated in Table 2. In July 2017, the a priori and a posteriori emission estimates are near identical for the MOPITT and IASI inversions. The July wildfire emissions were absent of any large wildfire smoke plumes. For North American anthropogenic emissions, the a posteriori estimates (4.5 Tg for MOPITT and 4.4 Tg for IASI) are lower than the a priori of 5.5 Tg.

In August 2017, the boreal North American wildfires presented an exceptional perturbation to wildfire CO emissions. The August 2017 a priori estimate is considerably greater than for July at 14.2 Tg and 5.8 Tg, respectively. The a posteriori estimate obtained from the MOPITT inversion is 14.4 Tg, which is a minor difference from the a priori. A reduction of emissions is observed in the a posteriori estimate for IASI, which is 11.4 Tg. However, both the a posteriori estimates for North American anthropogenic emissions in August are greater than for July. As anthropogenic CO sources have smoothly-varying seasonal variability, a marked increase in anthropogenic emissions is not expected from July to August. The differences may be largely attributed to the inability of the inversion to accurately distinguish between North American anthropogenic and wildfire sources. Due to the long-range transport of the wildfire smoke plumes, the westerly transport of these emissions also coincides with continental outflow of anthropogenic sources.

This misattribution is particularly evident for wildfire emission estimates from the boreal regions of boreal North America (BONA) and Asia (BOAS) due to their adjacent anthropogenic source regions, North America and Europe. For July, anthropogenic North American a posteriori emissions are 4.5 and 4.3 Tg for the MOPITT and IASI inversions, respectively, with an a priori of 5.5 Tg. Boreal North American a posteriori emissions are 5.8 Tg and 5.7 Tg for the MOPITT and IASI inversions, respectively, with a priori of 5.8 Tg. For August, an increase in the a posteriori North American anthropogenic emissions is observed, with the MOPITT and IASI inversions suggesting 5.8 Tg and 6.6 Tg, respectively. During the period of the 2017 Canadian wildfires in August, a slight increase in boreal North American wildfire emissions is observed in the a posteriori for MOPITT, while for IASI a decrease is observed. Considering net emissions from North America (a priori of 11.3 Tg and 19.7 Tg, for July and August, respectively), the total

Table 2. A priori and a posteriori emissions for the MOPITT and IASI inversions for August 2017. Global anthropogenic emissions are shown for all global sources, North America (NA) and Europe (EU). Biomass burning emissions are shown for boreal North America (BONA) and boreal Asia (BOAS)

July 2017

Emissions [Tg/month]	Global Biomass Burning	North America Anthro.	Boreal North America	Europe Anthro.	Boreal Asia
a priori	38.4	5.5	5.8	4.8	9.7
MOPITT a posteriori	45.0	4.5	5.8	4.9	9.3
IASI a posteriori	45.6	4.4	5.7	4.8	7.7

August 2017

Emissions [Tg/month]	Global Biomass Burning	North America Anthro.	Boreal North America	Europe Anthro.	Boreal Asia
a priori	53.6	5.5	14.2	4.8	8.2
MOPITT	73.3	5.8	14.4	5.6	7.9
IASI	70.7	6.6	11.4	5.6	6.5

a posteriori emissions from the MOPITT inversion are 10.1 Tg and 20.2 Tg for July and August, respectively. For IASI, the combined emissions are 10.0 Tg and 18.0 Tg, for July and August, respectively. For both instruments, the combined anthropogenic and wildfire a posteriori emissions are lower than the a priori.

Total anthropogenic and wildfire (BONA and TENA) a priori in the North American domain is 31 Tg for July to August. The a posteriori estimates are 30.5 Tg and 27.9 Tg for the MOPITT and IASI inversions, respectively, which are not notably different from the a priori. However, regional differences are present between the MOPITT and IASI inversions, as discussed in the following section.

3.3 Regional Analysis of the 2017 Canadian Wildfires

In this section, we focus on the two main wildfire emission hot-spots identified by Lutsch et al. (2019): British Columbia (BC) and Northwest Territories (NWT). These regions are shown in Figure 3 and the results of the MOPITT and IASI inversions are tabulated in Table 3. The BC and NWT hot-spots account for ∼70% of all wildfire emissions in North America for the month of August 2017. A posteriori emissions obtained from the MOPITT and IASI inversions show generally consistent results on continental-scales as shown in Table 2. The distinct differences between the two inversions are observed for the BC and NWT wildfires. The net a posteriori estimates in MOPITT and IASI inversions differ by ∼1.5 Tg for August, which is predominantly attributed to wildfires in BC and NWT, with a difference of 2.8 Tg. Differences in a posteriori estimates of other North American wildfire regions are negligible. Both inversions exhibit an increase in North American anthropogenic emissions from July to August which may be partly attributed to misrepresentation of wildfire emissions as anthropogenic.

To interpret these differences we need to consider the differences in the wildfire regimes and plume transport of the BC and NWT sources. The transport of these plumes was examined in Lutsch et al. (2019) using a back-trajectory analysis and the results are summarized here. The predominant wildfire emissions from these sources occurred in August 2017. A large plume originated in the BC region on 10 August 2017, which was transported northward to NWT, and combined with the NWT source on 14 August 2017. The combined plume was then transported poleward, where it reached the Eureka and Thule FTIR measurement sites on 19 August and 20 August, respectively. Through the back-

Table 3. a priori and a posteriori estimates for continental North American (NA) domain, and regional wildfire sources of British Columbia (BC) and the Northwest Territories (NWT)

July 2017				
Emissions [Tg/month]	North America Anthro.	North America BB	BC	NWT
a priori	5.5	7.1	2.2	0.8
MOPITT a posteriori	4.5	6.9	2.2	0.8
IASI a posteriori	4.3	6.8	2.4	0.8
August 2017				
Emissions [Tg/month]	North America Anthro.	North America BB	BC	NWT
a priori	5.5	16.1	3.1	7.9
MOPITT a posteriori	5.5	16.5	3.5	7.7
IASI a posteriori	6.6	14.0	2.8	5.6

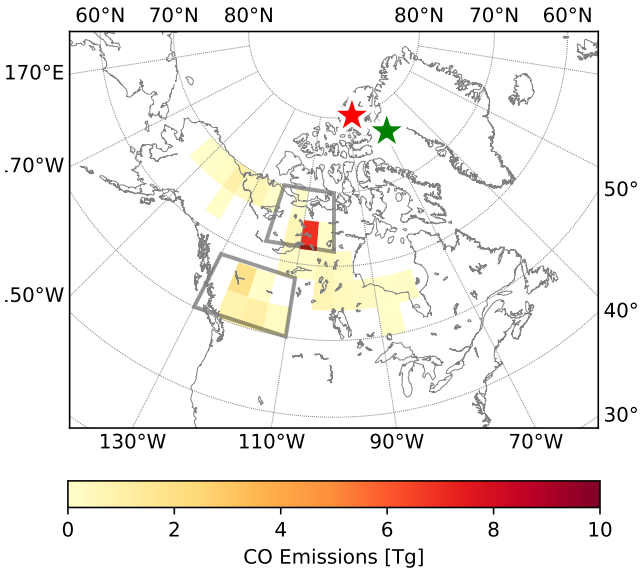

Figure 3. Cumulative July - August 2017 wildfire CO emissions over Canada. The black boxes indicate the BC (bottom) and NWT (top) wildfire source regions. Locations of the FTIR sites Eureka and Thule are shown by the red and green stars, respectively.

trajectory analysis, Lutsch et al. (2019) suggested the BC wildfire plumes influencing the FTIR measurement sites likely corresponded to the injection of the plume into the upper free-troposphere (>5 km), while the NWT plume corresponded to near-surface emissions, or injection into the lower free-troposphere (<5 km). Plume injection heights are provided by the GFASv1.2 emissions inventory. For the selected BC regions, a maximum plume top altitude of ∼8.5 km was reported for 10 August, with an August monthly mean of ∼4.5 km. For NWT, an August maximum plume top altitude of ∼3.6 km on 14 August was observed, with a monthly mean of 1.9 km. However, in the GEOS-Chem adjoint model, wildfire injection heights are not currently included, and wildfire emissions are released assuming a uniform distribution through the boundary layer.

To examine the impact of smoke plume injection heights on the inversion, a sensitivity test was performed as shown in Appendix C by evenly distributing the emissions from the surface to the daily maximum injection height from the GFASv1.2 inventory. The simulations illustrate that the inclusion of injection height information for the BC and NWT wildfire resulted in an insignificant contribution to the MOPITT inversion, and only a minor influence for IASI. While the inclusion of the injection height informa-

tion in the model may slightly improve the simulation of smoke plume transport, the inherent transport errors of the global coarse-resolution model are likely still the dominant source of smoke plume transport errors. A past study by Gonzi et al. (2011) had examined the sensitivity of MOPITT CO inversions to wildfire plume injection heights, and also concluded they had a minor influence on the a posteriori emissions.

A second sensitivity test was performed to further diagnose the ability of each instrument to constrain wildfire emissions. In this test, BONA wildfire emissions are perturbed by a factor of 2 and the results are summarized in Table D1. The results showed that both instruments were generally able to recover the a posteriori anthropogenic estimates of the truth from the unperturbed case of Table 3. For wildfires sources, the IASI inversion yielded a posteriori estimates closer to the the truth than MOPITT. This result suggests that the data assimilation of IASI measurements provides a better constraint of wildfire emissions. The contributions of each instrument's temporal coverage and vertical sensitivity are examined in Section 3.5.

3.4 Comparison Against Ground-based FTIR Measurements in the Arctic

Independent measurements of CO during the 2017 Canadian wildfires are scarce. Due to the transport of these plumes into the high-Arctic, observations are further limited due to the lack of dedicated observation sites in the region. Although there are a number surface-based measurement networks for CO, model comparisons to surface observations are prone to representativeness error. As shown by Lutsch et al. (2019), ground-based FTIR measurements during the 2017 Canadian wildfires were recorded in Eureka, Nunavut and Thule, Greenland as part of NDACC. Additional observations are provided at the Eureka site from TCCON measurements. The FTIR timeseries are shown in Figure 4.

All GEOS-Chem simulations show a general underestimation in comparison to the Eureka FTIR measurements on the fire-affected day of 19 August 2017. Consistent with the a posteriori emission estimates, the MOPITT a posteriori is nearly identical to the a priori, while the IASI a posteriori is more greatly underestimated in comparison to the Eureka FTIR measurements. As illustrated in Lutsch et al. (2019), Eureka was predominately influenced from 17-21 August 2017 by wildfire emissions originating in NWT. For

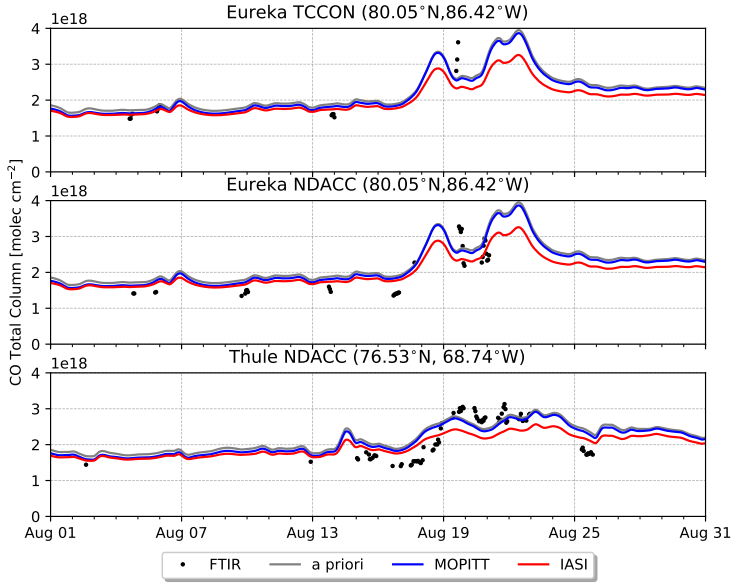

Figure 4. Hourly-averaged FTIR CO total columns for August 2017 at Eureka and Thule (black). The GEOS-Chem a priori timeseries (grey), MOPITT inversion (blue) and IASI (red) inversion timeseries are also shown.

Thule, there is some indication that GEOS-Chem captures the influence of the wildfire emissions during the period of enhanced FTIR measurements from 19–22 August. Thule was found to be predominately influenced by wildfire emissions originating in BC. As was the case for Eureka, the a posteriori estimates for MOPITT are nearly identical to the a priori, while the IASI a posteriori emission estimates leads to a further underestimation in comparison to the Thule FTIR measurements.

Although the GEOS-Chem to FTIR comparisons would suggest an underestimation of emissions from BC and NWT wildfire sources, it should be noted that inherit model errors may also contribute to this underestimation. Global models tend to suffer from numerical diffusion errors (Eastham and Jacob (2017); Rastigejev et al. (2010)) as a result of the coarse vertical and horizontal resolution. Numerical diffusion will contribute to errors in the simulated transport pathways of the plume, in addition to artificial loss of the tracer species. Additionally, the coarse model resolution leads to loss of vertical convection as a result of degrading the input meteorological fields from its native resolution (Yu et al., 2018). The poorly resolved vertical convection may lead to further errors in simulating the transport wildfire smoke plumes. However, these model errors will

also contribute to errors in the inversion itself, leading to uncertainties in the model a posteriori emissions, although these issues are inherent in the inversion.

3.5 Observing System Simulation Experiments (OSSEs)

To diagnose the sensitivity of the inversion to the observation coverage and vertical resolution of the observations, we perform several observing system simulation experiments (OSSEs). First, pseudo observations are generated by sampling the optimized CO states from the IASI inversion at the MOPITT and IASI measurement locations, in both space and time. These pseudo observations are then used for six OSSEs:

1. MOPITT sampled with an averaging kernel of unity applied.
2. IASI sampled with an averaging kernel of unity applied.
3. MOPITT sampled with MOPITT averaging kernel applied.
4. MOPITT sampled with IASI averaging kernel applied.
5. IASI sampled with MOPITT averaging kernel applied.
6. IASI sampled with IASI averaging kernel applied.

Cases (1) and (2) allow for the impact of the temporal coverage of the observations on the inversion to be quantified. Cases (3) and (4) provide a means to quantify the contribution of the averaging kernels with the temporal coverage of MOPITT. Similarly, Cases (5) and (6), will quantify the contribution of the averaging kernels with the greater temporal coverage of IASI.

Both the MOPITT and IASI measurement averaging kernels are spatially and temporally variable as they are dependent on the a priori CO profiles and true profiles of the measurement. However, the shape and magnitude of the averaging kernels of both instruments do not vary greatly. The averaging kernels of each instrument are distinct between the two. For the OSSE inversions, it is ideal to apply the true averaging kernel profiles of each instrument to the pseudo observations. Due to the different temporal coverage of MOPITT and IASI, it is not possible to match the pseudo observations to the instrument averaging kernels in Cases (4) and (6). To mitigate this issue, a mean averaging kernel is generated for each instrument by averaging all measurements globally for all of 2017. This method provides an idealized averaging kernel for each mea-

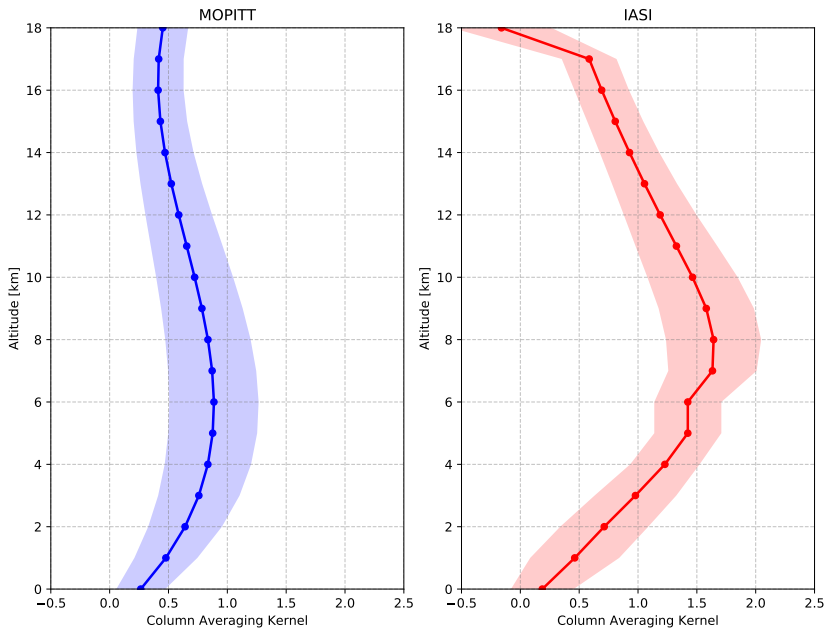

Figure 5. Global mean total column averaging kernels for 2017 of MOPITT and IASI CO measurements. The shaded region represents the standard deviation from the mean.

surement to be applied for all pseudo observations. These mean MOPITT and IASI averaging kernels are shown in Figure 5.

The mean MOPITT averaging kernel exhibits a fairly uniform distribution, with mean values between 0.5 and 1.0 through the troposphere and lower stratosphere. Minimal sensitivity to the surface is observed, with a mean value of approximately 0.2±0.2. The mean IASI averaging kernel exhibits a more pronounced peak through the mid- to upper-troposphere (∼4-12 km), with values exceeding 1.0 in this range. Although the magnitude of the mean averaging kernels of IASI and MOPITT differ as a result of the differences in their respective retrieval schemes, both instruments have sufficient vertical sensitivity in the free troposphere. Given the more pronounced peak of the IASI averaging kernels in the 4-12 km range, it is expected that the IASI assimilation should be more sensitive to transported wildfire emissions which are generally most abundant at these altitudes.

The results of the OSSEs are summarized in Table 4 and shown in Figure 6. For July 2017, wildfire emissions observed in the a priori and a posteriori of the truth are largely attributed to the BC wildfires, while anthropogenic emissions in North America

Table 4. Regional a priori and a posteriori emissions for the OSSEs. The value in the parentheses is the relative difference from the truth.

		July 2017			
OSSE	**Emissions [Tg/month]**	North America Anthro.	North America BB	BC	NWT
–	a priori	5.5	6.6	2.2	0.8
truth	a posteriori	4.4	6.4	2.4	0.7
1	MOPITT (AVK=1)	4.4 (0%)	6.1 (-5%)	2.0 (-20%)	0.8 (13%)
2	IASI (AVK=1)	4.4 (0%)	6.3 (-2%)	2.2 (-8%)	0.8 (13%)
3	MOPITT (AVK=MOPITT)	4.5 (2%)	6.2 (-3%)	2.0 (-20%)	0.8 (13%)
4	MOPITT (AVK=IASI)	4.6 (5%)	6.2 (-3%)	2.0 (-20%)	0.8 (13%)
5	IASI (AVK=MOPITT)	4.4 (0%)	6.2 (-3%)	2.2 (-8%)	0.8 (13%)
6	IASI (AVK=IASI)	4.3 (0%)	6.2 (-3%)	2.1 (-13%)	0.8 (13%)
		August 2017			
OSSE	**Emissions [Tg/month]**	North America Anthro.	North America BB	BC	NWT
–	a priori	5.5	15.2	3.2	7.9
truth	a posteriori	6.6	13.2	2.8	5.5
1	MOPITT (AVK=1)	5.9 (-11%)	14.9 (12%)	2.6 (-7%)	7.1 (29%)
2	IASI (AVK=1)	6.3 (-5%)	13.6 (3%)	2.7 (-4%)	6.5 (18%)
3	MOPITT (AVK=MOPITT)	5.9 (-11%)	14.2 (8%)	2.6 (-7%)	7.3 (32%)
4	MOPITT (AVK=IASI)	5.8 (-12%)	14.4 (9%)	2.6 (-7%)	7.5 (36%)
5	IASI (AVK=MOPITT)	6.2 (-6%)	13.8 (5%)	2.6 (-7%)	6.8 (24%)
6	IASI (AVK=IASI)	6.1 (-8%)	14.0 (6%)	2.5 (-10%)	7.0 (27%)

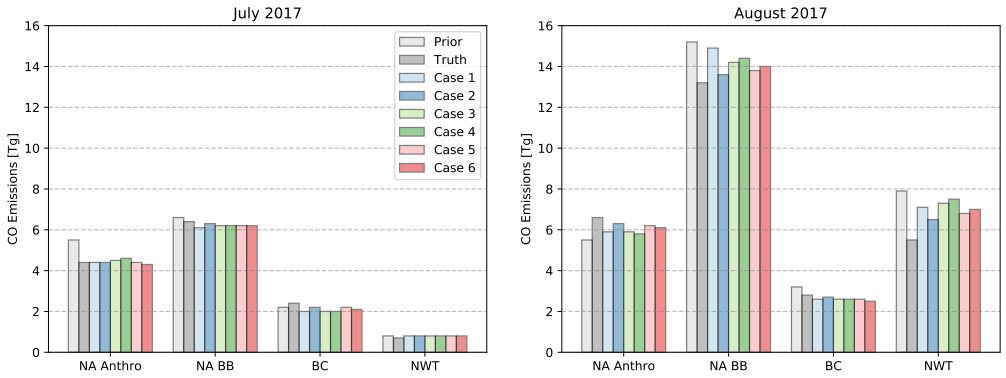

Figure 6. Regional a priori and a posteriori emissions for the OSSEs corresponding to Table 4.

519 are the predominant CO source. In all OSSEs, the a posteriori anthropogenic emissions
520 are similar to the truth, with absolute differences of 5% or less. Similarly, total wildfire
521 emissions of North America are also comparable to the truth, with absolute differences
522 of 5% or less. For BC, the a posteriori emissions of the OSSEs differ from the truth rang-
523 ing from 8% to 20%. Cases (1) and (2) yield the best agreement to the truth with an
524 8% overestimation. However, the a posteriori estimates of NWT are identical for all OSSEs.

525 For August 2017, total North American emissions are largely attributed to wild-
526 fire emissions. In all cases, a underestimation of North American anthropogenic emis-
527 sions is observed. For North American wildfire emissions, an overestimation is observed
528 in all OSSEs. BC wildfire emissions are underestimated in the OSSEs, while they are
529 overestimated for NWT. It should be noted that the magnitude of the differences in the
530 a posteriori estimates of the OSSEs is correlated with the magnitude of emissions, with
531 greater emissions resulting in greater differences.

532 Comparing Cases (1) and (2) indicates the relative impact of the spatial and tem-
533 poral coverage of MOPITT and IASI, respectively, for both North American anthropogenic
534 and wildfire emissions. For these continental regions, Case (2) provides the closest agree-
535 ment to the truth, indicating that greater temporal coverage is advantageous in constrain-
536 ing continental scale emissions. Similarly, IASI coverage (Case 2) provides better esti-
537 mates for the regional wildfire sources of BC and NWT, with the exception of NWT in
538 July, which is a small emission source. The combined impact of the instrument cover-

age and its vertical sensitivity is highlighted in Cases (3) to (6) for NWT in August, which result in poorer agreements with the assumption of a IASI averaging kernel, regardless of the instrument coverage. The averaging kernel only has a modest impact, while the instrument coverage is the main factor influencing the ability of the assimilation to constrain wildfire emissions.

The advantage of the greater temporal sampling of IASI is also observed in Table 4 and Figure 6. The greater temporal sampling better captures the transport of wildfire emissions in comparison to MOPITT, while providing a greater number of measurements near the wildfire sources. Therefore, IASI provides an improvement in the ability to resolve the episodic wildfire sources.

4 Summary

In this study, we examined the ability of MOPITT and IASI CO observations to constrain episodic boreal wildfire emissions using a case study of the 2017 Canadian wildfires. Global CO emission sources were optimized using data assimilation of MOPITT and IASI CO observations, respectively. As discussed in Section 3.1, the MOPITT and IASI inversions produced generally consistent posterior emissions globally (see Table 1). For the high-latitude boreal wildfire regions of BONA and BOAS, MOPITT a posteriori emissions were nearly identical to the a priori. The regional analysis presented in Section 3.2 of the high-latitude wildfire regions of BONA and BOAS suggest that both the MOPITT and IASI inversions partially attribute wildfire emissions in these regions to neighboring anthropogenic sources of North America and Europe, respectively. This result indicates that both the MOPITT and IASI instruments are unable to accurately constrain episodic boreal wildfire emissions.

The inability of MOPITT to constrain high-latitude wildfire emissions, while IASI provided some improvement, was further illustrated in the regional analysis of the 2017 Canadian wildfires of Section 3.3. Optimized wildfire emissions for the BC and NWT obtained from the MOPITT inversion were nearly identical to the a priori. In contrast, the IASI inversion yielded a slight reduction of the a posteriori wildfire emissions in BC and NWT from the a priori.

To identify the contribution of temporal converge and vertical sensitivity of each instrument, a series of OSSEs was performed as presented and discussed in Section 3.5.

For the BC and NWT wildfire sources, it was apparent that the greater temporal sampling of IASI consistently yielded a posteriori estimates that most closely replicated the truth. It was also observed that the vertical sensitivity of each instrument only had a minor contribution to the optimized emissions, whereas the MOPITT averaging kernel had a slight improvement over IASI.

The results of this study indicate that to constrain high-latitude boreal wildfire emissions in a global CTM, the frequency and spatial density of the measurements is more important than the surface sensitivity. However, the inherent model errors may also adversely impact the ability to accurately optimize high-latitude wildfire emissions. The use of a higher-spatial resolution model would mitigate transport errors that are prone at course resolution. In addition, the use of a high-resolution model will also serve to improve the accuracy of simulating smoke plume transport. The implementation of realistic wildfire emission injection heights would also be beneficial to improve this aspect of the model. Combined, these model improvements would enable more accurate estimates of wildfire emissions, while taking full advantage of IASI and future missions.

Appendix A Weak-constraint 4D-Var Data Assimilation

The 4D-Var assimilation scheme assumes the model is perfect and neglects the influence of model errors in the cost function. To account for the influence of model errors, a forcing term is added to the cost function of Equation 1:

$$J(\boldsymbol{x}_0, \boldsymbol{u}) = \sum_{i=1}^{N} \left[\mathbf{F}(\boldsymbol{x}) - \boldsymbol{z}_i\right]^T \mathbf{S}_\sigma^{-1} \left[\mathbf{F}(\boldsymbol{x}) - \boldsymbol{z}_i\right] + \left[\boldsymbol{x} - \boldsymbol{x}_0\right]^T \mathbf{B}^{-1} \left[\boldsymbol{x} - \boldsymbol{x}_0\right] + \sum_{i=1}^{N-1} \boldsymbol{u}_i^T \mathbf{Q}^{-1} \boldsymbol{u}_i, \quad \text{(A1)}$$

where $\mathbf{x}$ is the CO distribution, $\boldsymbol{x}_0$ is the initial CO distribution, $\mathbf{B}$ is the a priori covariance, $\boldsymbol{u}_i$ are the model forcing terms, and $\mathbf{Q}$ is the model a priori covariance matrix. The forcing terms have been assumed to be uncorrelated in time and uncorrelated to the estimated parameters and is updated every 6 days during the assimilation window. The model a priori covariance matrix $\mathbf{Q}$ is assumed to be constant. It should be noted that the terms the Equations 1 and A1 are nearly identical and therefore in the context of chemical data assimilation the forcing term may be thought of as artificial sources and sinks throughout the atmosphere. The assimilation is performed over a 3-month assim-

597 ilation window from 1 May - 1 July 2017 to generate an optimized CO distribution for
598 1 June 2017.

599 Column measurements of CO from MOPITT and IASI illustrate considerable dif-
600 ferences as shown by George et al. (2015). Column differences between the MOPIT v5-
601 TIR and the IASI v5T v20100815 retrievals are generally slightly higher over land with
602 bias ranging from 0 to 13%. The MOPITT-IASI bias also exhibited a seasonal and lat-
603 itudinal dependence. Biases in the total column CO measurements of the MOPITT v8J
604 and IASI v20140922 have yet to be quantified. However, the initial model distribution
605 is optimized for each instrument therefore partially mitigating the impact of the instru-
606 ment biases in the inversion. The optimized initial states for MOPITT and IASI are shown
607 in Figure A1.

608 Appendix B Consideration of Measurement Averaging Kernels

609 Averaging kernels represent the sensitivity of the measurement information con-
610 tent provided by the measurement or a priori. It is essential that the averaging kernel
611 is taken into account for the assimilation scheme. For both the MOPITT and IASI in-
612 versions, the averaging kernels are applied as follows.

613 B1 MOPITT averaging kernels

614 The model state matching the MOPITT observation in both space and time is smoothed
615 by the MOPITT averaging kernel:

$$\hat{x} = \boldsymbol{h}^T \boldsymbol{x}_a + \boldsymbol{a}^T \left[\log(\boldsymbol{x}) - \log(\boldsymbol{x}_a)\right], \tag{B1}$$

616 where $\hat{x}$ is the smoothed model column (in units of molec cm^{-2}), $\mathbf{h}$ is the column op-
617 erator (in units of molec cm^{-2}), $\mathbf{a}$ is the MOPITT total column averaging kernel (in units
618 of molec cm^{-2}), and $\mathbf{x}$ and $\mathbf{x}_a$ are the model and a priori MOPITT VMR profiles, re-
619 spectively. Each vector has a length of 10 corresponding to the number of levels in the
620 MOPITT retrieval grid. As such, the model profiles are first binned from their 47-layer
621 grid to the 10-layer MOPITT grid.

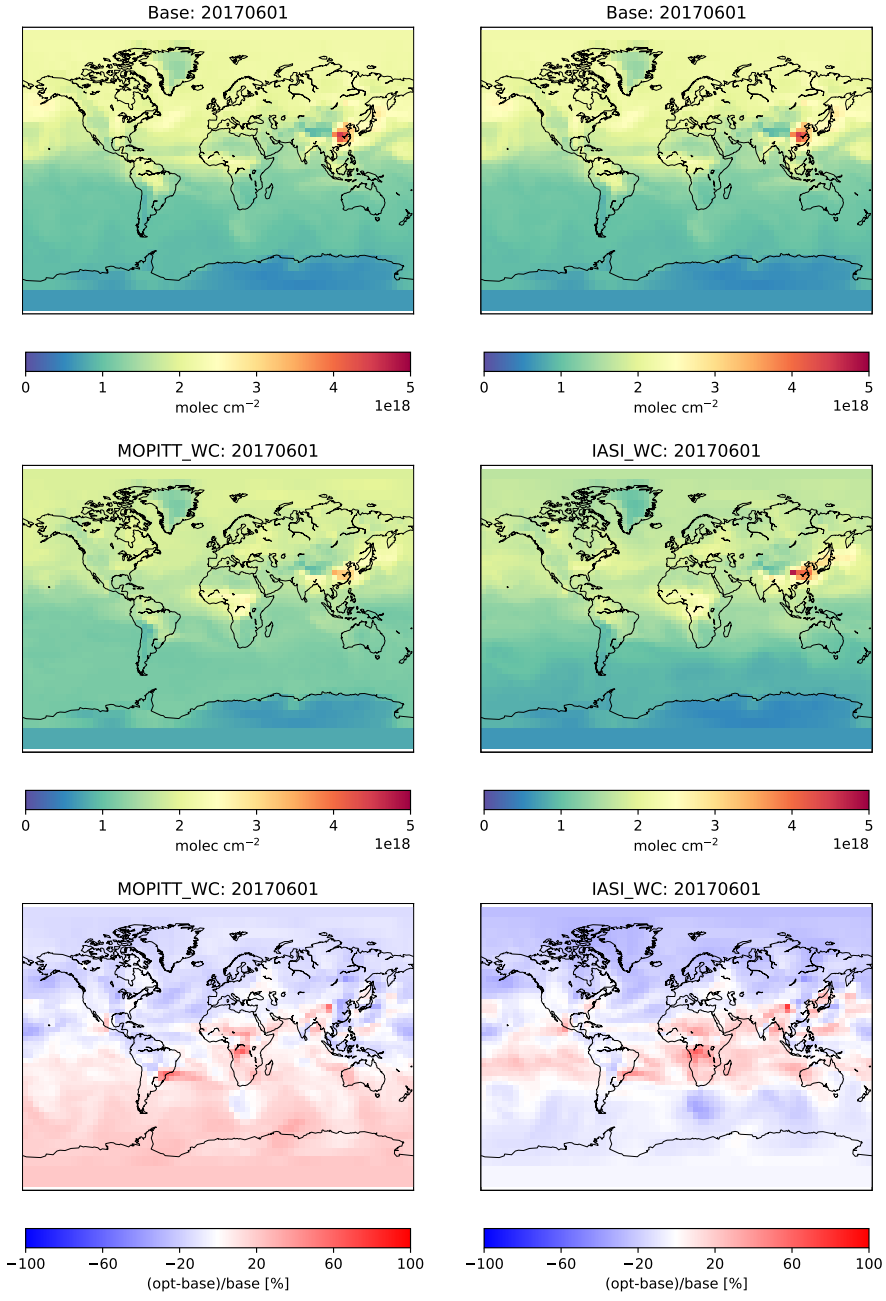

Figure A1. 1 June 2017 daily-mean a priori (top) and a posteriori (middle) CO states and a posteriori-a priori relative difference for the MOPITT and IASI CO state optimizations.

B2 IASI Averaging Kernels

For IASI, the averaging kernel is applied in a similar method to MOPITT. The model column is smoothed by the IASI averaging kernel:

$$\hat{x} = x_a + \boldsymbol{a}^T \left[\boldsymbol{x} - \boldsymbol{x}_a\right], \tag{B2}$$

where $\hat{x}$ is the smoothed model column (in units of molec cm^{-2}), $\boldsymbol{a}$ is the IASI total column averaging kernel (unitless), $\boldsymbol{x}$ and $\boldsymbol{x}_a$ are the model and IASI a priori partial column profiles (in units of molec cm^{-2}), respectively. Each vector has a length of 19 corresponding to the number of levels in the IASI retrieval grid. As such, the model profiles are first binned from their 47-layer grid to the 19-layer IASI grid.

Appendix C Sensitivity of Inversion to Boreal Wildfire Injection Heights

Since wildfire emissions are commonly injected into the free troposphere, the assumption of emissions being distributed through the planetary boundary layer may not always be realistic. This assumption may also contribute further model plume transport errors in addition to the inherent model transport errors. To investigate the influence of wildfire emission injection heights, we performed a sensitivity test by injecting emissions based on archived plume injection heights from the GFASv1.2 emission inventory mean altitude of maximum injection (MAMI) product. Modeled emissions were then distributed evenly from the surface to the daily maximum MAMI value in each $4°\times5°$ horizontal grid box. The results of MOPITT and IASI inversions are tabulated in Table C1.

Table C1. A priori and a posteriori estimates for continental North American (NA) domain, and regional wildfire sources of British Columbia (BC) and the Northwest Territories (NWT) for the sensitivity test with a priori BONA wildfire emissions injected to the GFAS MAMI values. Differences in the emissions from the true case of Table 3 are shown in parentheses.

	July 2017			
Emissions [Tg/month]	North America Anthro.	North America BB	BC	NWT
a priori	5.5 (0)	7.1 (0)	2.2 (0)	0.8 (0)
MOPITT a posteriori	4.7 (0.2)	6.7 (0)	2.1 (0.1)	0.8 (0)
IASI a posteriori	4.3 (0.1)	6.5 (-0.3)	2.1 (0.3)	0.8 (0)
	August 2017			
Emissions [Tg/month]	North America Anthro.	North America BB	BC	NWT
a priori	5.5 (0)	16.1 (0)	3.1 (0)	7.9 (0)
MOPITT a posteriori	5.4 (-0.4)	16.3 (-0.1)	3.5 (-0.2)	7.7 (0.2)
IASI a posteriori	4.3 (-0.1)	15.0 (1.1)	2.9 (0.1)	6.5 (1.1)

manuscript submitted to *JGR: Atmospheres*

Appendix D Sensitivity of the Inversion to A Priori Boreal Wildfire Emissions

In the inversion system, the a posteriori emission estimates are sensitive to the a priori. In the case of boreal wildfire emissions, these episodic events occur on short-term timesecales, on the order of several weeks and unlike anthropogenic emissions, boreal wildfires are subject to a high degree of variability. Total monthly emissions from boreal wildfires may be comparable to or exceed those of nearby anthropogenic sources. The combination of the measurement uncertainty and model errors contribute to model noise, and as such, the wildfire emission signal may be comparable to the model noise. As a result, the inversion may lack the sensitivity to effectively constrain these emissions.

To examine the sensitivity of the MOPITT and IASI inversions to boreal wildfire emissions, we perform a sensitivity experiment to quantify this impact. To do so, BONA wildfire emissions are scaled by a factor of 2 for the assimilation window from 1 June - 1 October 2017. As the perturbed emissions may be unphysically large, the global a priori covariance was also increased from 50% to 100%. The inversion results are tabulated in Table D1.

Table D1. A priori and a posteriori estimates for continental North American (NA) domain, and regional wildfire sources of British Columbia (BC) and the Northwest Territories (NWT) for the sensitivity test with a priori BONA wildfire emissions being scaled by a factor of 2. Differences in the emissions from the true case of Table 3 are shown in parentheses.

		July 2017		
Emissions [Tg/month]	North America Anthro.	North America BB	BC	NWT
a priori	5.5 (0)	13.6 (6.5)	4.2 (2.2)	1.6 (0.8)
MOPITT a posteriori	3.4 (-1.1)	10.6 (3.7)	3.0 (0.8)	1.4 (0.6)
IASI a posteriori	4.2 (-0.1)	9.1 (2.3)	3.1 (0.7)	1.2 (0.5)
		August 2017		
Emissions [Tg/month]	North America Anthro.	North America BB	BC	NWT
a priori	5.5 (0)	31.6 (15.6)	6.3 (3.1)	15.8 (7.9)
MOPITT a posteriori	5.4 (-0.5)	26.3 (9.8)	4.9 (1.3)	13.2 (5.5)
IASI a posteriori	6.5 (-0.1)	17.9 (4.0)	4.0 (1.2)	4.7 (-0.8)

manuscript submitted to *JGR: Atmospheres*

Acknowledgments

This project was undertaken with the financial support of the Canadian Space Agency (CSA) through the Earth System Science Data Analyses program (grant no. 16SUAS-COBF). The MOPITT team acknowledges support from the Canadian Space Agency (CSA), the Natural Sciences and Engineering Research Council (NSERC) and Environment and Climate Change Canada (ECCC), along with the contributions of COMDEV and ABB BOMEM. The NCAR MOPITT project is supported by the National Aeronautics and Space Administration (NASA) Earth Observing System (EOS) Program. IASI is a joint mission of EUMETSAT and the Centre National d'Etudes Spatiales (CNES, France). The authors acknowledge the AERIS data infrastructure for providing access to the IASI data in this study, ULB-LATMOS for the development of the retrieval algorithms, and Eumetsat/AC SAF for CO data production. Bruker FTIR measurements were made at PEARL by the Canadian Network for the Detection of Atmospheric Composition Change (CANDAC), which has been supported by the Atlantic Innovation Fund/Nova Scotia Research Innovation Trust, Canada Foundation for Innovation, Canadian Foundation for Climate and Atmospheric Sciences, CSA, ECCC, Government of Canada International Polar Year funding, NSERC, Northern Scientific Training Program, Ontario Innovation Trust, Polar Continental Shelf Program, and Ontario Research Fund. The National Center for Atmospheric Research is sponsored by the National Science Foundation. The NCAR FTS observation programs at Thule, GR is supported under contract by the National Aeronautics and Space Administration (NASA). The Thule work is also supported by the NSF Office of Polar Programs (OPP). We wish to thank the Danish Meteorological Institute for support at the Thule site.

Data Availability: MOPITT Version 8 data are freely available at `https://earthdata.nasa.gov/`. The IASI Level-2 CO data are provided by the Aeris data infrastructure and are available at `https://www.aeris-data.fr/`. The NDACC CO measurements are available from the NDACC database hosted by NOAA at `https://www-air.larc.nasa.gov/missions/ndacc/data.html` and the Eureka TCCON measurements are available at `https://tccondata.org`. The authors acknowledge the use of the GFASv1.2 emissions inventory, which contains modified Copernicus Atmosphere Monitoring Service information (2018). The GEOS data used in this study have been provided by the Global Modeling and Assimilation Office (GMAO) at NASA Goddard Space Flight Center.

References

Akagi, S. K., Yokelson, R. J., Wiedinmyer, C., Alvarado, M. J., Reid, J. S., Karl, T., ... Wennberg, P. O. (2011, May). Emission factors for open and domestic biomass burning for use in atmospheric models. *Atmospheric Chemistry and Physics*, *11*(9), 4039-4072. doi: 10.5194/acp-11-4039-2011

Amiro, B. D., Cantin, A., Flannigan, & de Groot, W. J. (2009, February). Future emissions from Canadian boreal forest fires. *Canadian Journal of Forest Research. Journal Canadien de la Recherche Forestiere*, *39*(2), 383-395. doi: 10.1139/X08-154

Andreae, M. O. (2019, July). Emission of trace gases and aerosols from biomass burning – an updated assessment. *Atmospheric Chemistry and Physics*, *19*(13), 8523-8546. doi: 10.5194/acp-19-8523-2019

Andreae, M. O., & Merlet, P. (2001, December). Emission of trace gases and aerosols from biomass burning. *Global Biogeochemical Cycles*, *15*(4), 955-966. doi: 10.1029/2000GB001382

Arellano, A. F. (2004). Top-down estimates of global CO sources using MOPITT measurements. *Geophysical Research Letters*, *31*(1). doi: 10.1029/2003gl018609

Aumann, H. H., Chahine, M. T., Gautier, C., Goldberg, M. D., Kalnay, E., McMillin, L. M., ... Susskind, J. (2003, February). AIRS/AMSU/HSB on the Aqua mission: design, science objectives, data products, and processing systems. *IEEE Transactions on Geoscience and Remote Sensing: a Publication of the IEEE Geoscience and Remote Sensing Society*, *41*(2), 253-264. doi: 10.1109/TGRS.2002.808356

Barré, J., Edwards, D., Worden, H., Da Silva, A., & Lahoz, W. (2015, July). On the feasibility of monitoring carbon monoxide in the lower troposphere from a constellation of Northern Hemisphere geostationary satellites. (Part 1). *Atmospheric environment*, *113*, 63-77. doi: 10.1016/j.atmosenv.2015.04.069

Barré, J., Gaubert, B., Arellano, A. F. J., Worden, H. M., Edwards, D. P., Deeter, M. N., ... Hurtmans, D. (2015). Assessing the impacts of assimilating IASI and MOPITT CO retrievals using CESM-CAM-chem and DART. *Journal of Geophysical Research, D: Atmospheres*, *120*(19), 10,501-10,529. doi: 10.1002/2015JD023467

721 Bond-Lamberty, B., Peckham, S. D., Ahl, D. E., & Gower, S. T. (2007, November).
722 Fire as the dominant driver of central Canadian boreal forest carbon balance.
723 *Nature*, *450*(7166), 89-92. doi: 10.1038/nature06272

724 Buchholz, R. R., Deeter, M. N., Worden, H. M., Gille, J., Edwards, D. P., Hanni-
725 gan, J. W., ... Langerock, B. (2017, June). Validation of MOPITT carbon
726 monoxide using ground-based Fourier transform infrared spectrometer data
727 from NDACC. *Atmospheric Measurement Techniques*, *10*(5), 1927-1956. doi:
728 10.5194/amt-10-1927-2017

729 Clerbaux, C., Boynard, A., Clarisse, L., George, M., Hadji-Lazaro, J., Herbin, H.,
730 ... Coheur, P.-F. (2009, August). Monitoring of atmospheric composition
731 using the thermal infrared IASI/MetOp sounder. *Atmospheric Chemistry and*
732 *Physics*, *9*(16), 6041-6054. doi: 10.5194/acp-9-6041-2009

733 Clerbaux, C., George, M., Turquety, S., Walker, K. A., Barret, B., Bernath, P., ...
734 Wiacek, A. (2008, May). CO measurements from the ACE-FTS satellite
735 instrument: data analysis and validation using ground-based, airborne and
736 spaceborne observations. *Atmospheric Chemistry and Physics*, *8*(9), 2569-
737 2594. doi: 10.5194/acp-8-2569-2008

738 Deeter, M. N. (2003). Operational carbon monoxide retrieval algorithm and selected
739 results for the MOPITT instrument. *Journal of Geophysical Research: Atmo-*
740 *spheres*, *108*(D14). doi: 10.1029/2002jd003186

741 Deeter, M. N., Edwards, D. P., Francis, G. L., Gille, J. C., Mao, D., Martínez-
742 Alonso, S., ... Andreae, M. O. (2019). Radiance-based retrieval bias mit-
743 igation for the MOPITT instrument: the version 8 product. *Atmospheric*
744 *Measurement Techniques*, *12*(8), 4561-4580. doi: 10.5194/amt-12-4561-2019

745 Deeter, M. N., Edwards, D. P., Francis, G. L., Gille, J. C., Martínez-Alonso, S.,
746 Worden, H. M., & Sweeney, C. (2017, July). A climate-scale satellite record for
747 carbon monoxide: the MOPITT Version 7 product. *Atmospheric Measurement*
748 *Techniques*, *10*(7), 2533-2555. doi: 10.5194/amt-10-2533-2017

749 Deeter, M. N., Edwards, D. P., Gille, J. C., Emmons, L. K., Francis, G., Ho, S.-
750 P., ... Novelli, P. C. (2010, April). The MOPITT version 4 CO product:
751 Algorithm enhancements, validation, and long-term stability. *Journal of Geo-*
752 *physical Research: Atmospheres*, *115*(D7). doi: 10.1029/2009jd013005

753 Deeter, M. N., Martínez-Alonso, S., Edwards, D. P., Emmons, L. K., Gille, J. C.,

754 Worden, H. M., ... Wofsy, S. C. (2014, November). The MOPITT Version 6
755 product: algorithm enhancements and validation. *Atmospheric Measurement*
756 *Techniques*, *7*(11), 3623-3632. doi: 10.5194/amt-7-3623-2014

757 de Groot, W. J., Flannigan, M. D., & Cantin, A. S. (2013, April). Climate change
758 impacts on future boreal fire regimes. *Forest Ecology and Management*, *294*,
759 35-44. doi: 10.1016/j.foreco.2012.09.027

760 De Mazière, M., Thompson, A. M., Kurylo, M. J., Wild, J. D., Bernhard, G., Blu-
761 menstock, T., ... Strahan, S. E. (2018, April). The Network for the De-
762 tection of Atmospheric Composition Change (NDACC): history, status and
763 perspectives. *Atmospheric Chemistry and Physics*, *18*(7), 4935-4964. doi:
764 10.5194/acp-18-4935-2018

765 De Wachter, E., Barret, B., Le Flochmoën, E., Pavelin, E., Matricardi, M., Cler-
766 baux, C., ... Cammas, J. P. (2012, November). Retrieval of MetOp-A/IASI
767 CO profiles and validation with MOZAIC data. *Atmospheric Measurement*
768 *Techniques*, *5*(11), 2843-2857. doi: 10.5194/amt-5-2843-2012

769 Drummond, J. R., Zou, J., Nichitiu, F., Kar, J., Deschambaut, R., & Hackett,
770 J. (2010, March). A review of 9-year performance and operation of the
771 MOPITT instrument. *Advances in Space Research*, *45*(6), 760-774. doi:
772 10.1016/j.asr.2009.11.019

773 Eastham, S. D., & Jacob, D. J. (2017, February). Limits on the ability of global
774 Eulerian models to resolve intercontinental transport of chemical plumes. *At-*
775 *mospheric Chemistry and Physics*, *17*(4), 2543-2553. doi: 10.5194/acp-17-2543
776 -2017

777 Fortems-Cheiney, A., Chevallier, F., Pison, I., Bousquet, P., Szopa, S., Deeter,
778 M. N., & Clerbaux, C. (2011, March). Ten years of CO emissions as seen
779 from Measurements of Pollution In The Troposphere (MOPITT). *Journal of*
780 *Geophysical Research: Atmospheres*, *116*(D5). doi: 10.1029/2010jd014416

781 Fu, D., Bowman, K. W., Worden, H. M., Natraj, V., Worden, J. R., Yu, S., ... Han,
782 Y. (2016). High-resolution tropospheric carbon monoxide profiles retrieved
783 from CrIS and TROPOMI. *Atmospheric Measurement Techniques*, *9*(6),
784 2567-2579. doi: 10.5194/amt-9-2567-2016

785 George, M., Clerbaux, C., Bouarar, I., Coheur, P.-F., Deeter, M. N., Edwards,
786 D. P., ... Worden, H. M. (2015, October). An examination of the long-

term CO records from MOPITT and IASI: comparison of retrieval methodology. *Atmospheric Measurement Techniques*, *8*(10), 4313-4328. doi: 10.5194/amt-8-4313-2015

Gonzi, S., Feng, L., & Palmer, P. I. (2011, April). Seasonal cycle of emissions of CO inferred from MOPITT profiles of CO: Sensitivity to pyroconvection and profile retrieval assumptions. *Geophysical Research Letters*, *38*(8). doi: 10.1029/2011gl046789

Guenther, A., Karl, T., Harley, P., Wiedinmyer, C., Palmer, P. I., & Geron, C. (2006, August). Estimates of global terrestrial isoprene emissions using MEGAN (model of emissions of gases and aerosols from nature). *Atmospheric Chemistry and Physics*, *6*(11), 3181-3210. doi: 10.5194/acp-6-3181-2006

Heald, C. L., Jacob, D. J., Jones, D. B. A., Palmer, P. I., Logan, J. A., Streets, D. G., ... Nehrkorn, T. (2004, December). Comparative inverse analysis of satellite (MOPITT) and aircraft (TRACE-P) observations to estimate Asian sources of carbon monoxide. *Journal of Geophysical Research: Atmospheres*, *109*(D23). doi: 10.1029/2004jd005185

Hedelius, J. K., He, T.-L., Jones, D. B. A., Baier, B. C., Buchholz, R. R., Mazière, M. D., ... Wunch, D. (2019, October). Evaluation of MOPITT Version 7 joint TIR–NIR X_{CO} retrievals with TCCON. *Atmospheric Measurement Techniques*, *12*(10), 5547-5572. doi: 10.5194/amt-12-5547-2019

Hurtmans, D., Coheur, P.-F., Wespes, C., Clarisse, L., Scharf, O., Clerbaux, C., ... Turquety, S. (2012, July). FORLI radiative transfer and retrieval code for IASI. *Journal of Quantitative Spectroscopy & Radiative Transfer*, *113*(11), 1391-1408. doi: 10.1016/j.jqsrt.2012.02.036

Inness, A., Baier, F., Benedetti, A., Bouarar, I., Chabrillat, S., Clark, H., ... the MACC team (2013, April). The MACC reanalysis: an 8 yr data set of atmospheric composition. *Atmospheric Chemistry and Physics*, *13*(8), 4073-4109. doi: 10.5194/acp-13-4073-2013

Inness, A., Blechschmidt, A.-M., Bouarar, I., Chabrillat, S., Crepulja, M., Engelen, R. J., ... Zerefos, C. (2015, May). Data assimilation of satellite-retrieved ozone, carbon monoxide and nitrogen dioxide with ECMWF's Composition-IFS. *Atmospheric Chemistry and Physics*, *15*(9), 5275-5303. doi: 10.5194/acp-15-5275-2015

Jiang, Z., Jones, D. B. A., Kopacz, M., Liu, J., Henze, D. K., & Heald, C. (2011, August). Quantifying the impact of model errors on top-down estimates of carbon monoxide emissions using satellite observations. *Journal of Geophysical Research: Atmospheres*, *116*(D15), D15S03. doi: 10.1029/2010JD015282

Jiang, Z., Jones, D. B. A., Worden, H. M., & Henze, D. K. (2015, February). Sensitivity of top-down CO source estimates to the modeled vertical structure in atmospheric CO. *Atmospheric Chemistry and Physics*, *15*(3), 1521-1537. doi: 10.5194/acp-15-1521-2015

Jiang, Z., Worden, J. R., Worden, H., Deeter, M., Jones, D. B. A., Arellano, A. F., & Henze, D. K. (2017). A 15-year record of CO emissions constrained by MOPITT CO observations. *Atmospheric Chemistry and Physics*, *17*(7), 4565-4583. doi: 10.5194/acp-17-4565-2017

Kaiser, J. W., Heil, A., Andreae, M. O., Benedetti, A., Chubarova, N., Jones, L., ... van der Werf, G. R. (2012, January). Biomass burning emissions estimated with a global fire assimilation system based on observed fire radiative power. *Biogeosciences*, *9*(1), 527-554. doi: 10.5194/bg-9-527-2012

Kasischke, E. S., & Turetsky, M. R. (2006). Recent changes in the fire regime across the North American boreal region - Spatial and temporal patterns of burning across Canada and Alaska. *Geophysical Research Letters*, *33*(9). doi: 10.1029/2006gl025677

Kerzenmacher, T., Dils, B., Kumps, N., Blumenstock, T., Clerbaux, C., Coheur, P.-F., ... Mazière, M. D. (2012, November). Validation of IASI FORLI carbon monoxide retrievals using FTIR data from NDACC. *Atmospheric Measurement Techniques*, *5*(11), 2751-2761. doi: 10.5194/amt-5-2751-2012

Khaykin, S. M., Godin-Beekmann, S., Hauchecorne, A., Pelon, J., Ravetta, F., & Keckhut, P. (2018, February). Stratospheric smoke with unprecedentedly high backscatter observed by lidars above southern France. *Geophysical Research Letters*, *45*(3), 1639-1646. doi: 10.1002/2017GL076763

Koster, R. D., Darmenov, A. S., & da Silva, A. M. (2015, September). The Quick Fire Emissions Dataset (QFED): Documentation of Versions 2.1, 2.2 and 2.4. Volume 38; Technical Report Series on Global Modeling and Data Assimilation [Computer software manual].

Kuhns, H., Knipping, E. M., & Vukovich, J. M. (2005). Development of a United

States-Mexico Emissions inventory for the Big Bend Regional Aerosol and Visibility Observational (BRAVO) study. *Journal of the Air & Waste Management Association*, *55*(5), 677-692. doi: 10.1080/10473289.2005.10464648

Lamarque, J.-F., Emmons, L. K., Hess, P. G., Kinnison, D. E., Tilmes, S., Vitt, F., ... Tyndall, G. K. (2012, March). CAM-chem: description and evaluation of interactive atmospheric chemistry in the Community Earth System Model. *Geoscientific Model Development*, *5*(2), 369-411. doi: 10.5194/gmd-5-369-2012

Landgraf, J., aan de Brugh, J., Scheepmaker, R., Borsdorff, T., Hu, H., Houweling, S., ... Hasekamp, O. (2016, October). Carbon monoxide total column retrievals from TROPOMI shortwave infrared measurements. *Atmospheric Measurement Techniques*, *9*(10), 4955-4975. doi: 10.5194/amt-9-4955-2016

Law, K. S., & Stohl, A. (2007, March). Arctic air pollution: origins and impacts. *Science*, *315*(5818), 1537-1540. doi: 10.1126/science.1137695

Li, F., Lawrence, D. M., & Bond-Lamberty, B. (2017, April). Impact of fire on global land surface air temperature and energy budget for the 20th century due to changes within ecosystems. *Environmental Research Letters*, *12*(4), 044014. doi: 10.1088/1748-9326/aa6685

Lutsch, E., Strong, K., Jones, D. B. A., Blumenstock, T., Conway, S., Fisher, J. A., ... Warneke, T. (2020, November). Detection and attribution of wildfire pollution in the Arctic and northern midlatitudes using a network of Fourier-transform infrared spectrometers and GEOS-Chem. *Atmospheric Chemistry and Physics*, *20*(21), 12813-12851. doi: 10.5194/acp-20-12813-2020

Lutsch, E., Strong, K., Jones, D. B. A., Ortega, I., Hannigan, J. W., Dammers, E., ... Fisher, J. A. (2019, July). Unprecedented atmospheric ammonia concentrations detected in the high Arctic from the 2017 Canadian Wildfires. *Journal of Geophysical Research: Atmospheres*, *124*(14), 8178-8202. doi: 10.1029/2019JD030419

Miyazaki, K., Eskes, H. J., & Sudo, K. (2012, March). Global NO_x emission estimates derived from an assimilation of OMI tropospheric NO_2 columns. *Atmospheric Chemistry and Physics*, *12*(5), 2263-2288. doi: 10.5194/acp-12-2263-2012

Muller, J. F., Stavrakou, T., Bauwens, M., George, M., Hurtmans, D., Coheur, P.-

F., ... Sweeney, C. (2018, February). Top-Down CO Emissions Based On IASI Observations and Hemispheric Constraints on OH Levels. *Geophysical Research Letters*, *45*(3), 1621-1629. doi: 10.1002/2017GL076697

Olivier, J. G. J., & Berdowski, J. J. M. (2001). Global emissions sources and sinks. the climate system. *Lisse, The Netherlands: AA Balkema Publishers/Swets & Zeitlinger Publishers*, *5809*(255), 33-78.

Patra, P. K., Houweling, S., Krol, M., Bousquet, P., Belikov, D., Bergmann, D., ... Wilson, C. (2011, December). TransCom model simulations of CH_4 and related species: Linking transport, surface flux and chemical loss with CH_4 variability in the troposphere and lower stratosphere. *Atmospheric Chemistry and Physics*, *11*(24), 12813-12837. doi: 10.5194/acp-11-12813-2011

Peterson, D. A., Campbell, J. R., Hyer, E. J., Fromm, M. D., Kablick, G. P., Cossuth, J. H., & DeLand, M. T. (2018, August). Wildfire-driven thunderstorms cause a volcano-like stratospheric injection of smoke. *npj Climate and Atmospheric Science*, *1*(1), 30. doi: 10.1038/s41612-018-0039-3

Pfister, G., Hess, P. G., Emmons, L. K., Lamarque, J. F., Wiedinmyer, C., Edwards, D. P., ... Sachse, G. W. (2005). Quantifying CO emissions from the 2004 Alaskan wildfires using MOPITT CO data. *Geophysical Research Letters*, *32*(11), 955. doi: 10.1029/2005GL022995

Philip, S., Martin, R. V., & Keller, C. A. (2016, May). Sensitivity of chemistry-transport model simulations to the duration of chemical and transport operators: a case study with GEOS-Chem v10-01. *Geoscientific Model Development*, *9*(5), 1683-1695. doi: 10.5194/gmd-9-1683-2016

Ranjbar, K., O'Neill, N. T., Lutsch, E., McCullough, E. M., AboEl-Fetouh, Y., Xian, P., ... Abboud, I. (2019, December). Extreme smoke event over the high Arctic. *Atmospheric Environment*, *218*, 117002. doi: 10.1016/j.atmosenv.2019.117002

Rastigejev, Y., Park, R., Brenner, M. P., & Jacob, D. J. (2010, January). Resolving intercontinental pollution plumes in global models of atmospheric transport. *Journal of Geophysical Research: Atmospheres*, *115*(D2), 4164. doi: 10.1029/2009JD012568

Rodgers, C. D. (2000). *Inverse methods for atmospheric sounding: Theory and practice*. World Scientific.

Rodgers, C. D., & Connor, B. J. (2003, February). Intercomparison of remote sounding instruments. *Journal of Geophysical Research: Atmospheres*, *108*(D3), 4116. doi: 10.1029/2002JD002299

Shindell, D. T., Chin, M., Dentener, F., Doherty, R. M., Faluvegi, G., Fiore, A. M., ... Others (2008). A multi-model assessment of pollution transport to the Arctic. *Atmospheric Chemistry and Physics*, *8*(17), 5353-5372. doi: 10.5194/acp-8-5353-2008

Spivakovsky, C. M., Logan, J. A., Montzka, S. A., Balkanski, Y. J., Foreman-Fowler, M., Jones, D. B. A., ... McElroy, M. B. (2000, April). Three-dimensional climatological distribution of tropospheric OH: Update and evaluation. *Journal of Geophysical Research: Atmospheres*, *105*(D7), 8931-8980. doi: 10.1029/1999JD901006

Stanevich, I., Jones, D. B. A., Strong, K., Keller, M., Henze, D. K., Parker, R. J., ... Deng, F. (2021, June). Characterizing model errors in chemical transport modeling of methane: using GOSAT XCH_4 data with weak-constraint four-dimensional variational data assimilation. *Atmospheric Chemistry and Physics*, *21*(12), 9545-9572. doi: 10.5194/acp-21-9545-2021

Stohl, A. (2006). Characteristics of atmospheric transport into the Arctic troposphere. *Journal of Geophysical Research: Atmospheres*, *111*(D11), 8355. doi: 10.1029/2005JD006888

Strong, K., Roche, S., Franklin, J. E., Mendonca, J., Lutsch, E., Weaver, D., ... Lindenmaier, R. (2019). *TCCON data from Eureka (CA), Release GGG2014.R3.* CaltechDATA. doi: 10.14291/TCCON.GGG2014.EUREKA01.R3

Turquety, S., Hurtmans, D., Hadji-Lazaro, J., Coheur, P.-F., Clerbaux, C., Josset, D., & Tsamalis, C. (2009, July). Tracking the emission and transport of pollution from wildfires using the IASI CO retrievals: analysis of the summer 2007 Greek fires. *Atmospheric Chemistry and Physics*, *9*(14), 4897-4913. doi: 10.5194/acp-9-4897-2009

Val Martin, M., Kahn, R. A., & Tosca, M. G. (2018, October). A global analysis of wildfire smoke injection heights derived from Space-Based Multi-Angle imaging. *Remote Sensing*, *10*(10), 1609. doi: 10.3390/rs10101609

Val Martin, M., Logan, J. A., Kahn, R. A., Leung, F.-Y., Nelson, D. L., & Diner,

952 D. J. (2010, February). Smoke injection heights from fires in North Amer-
953 ica: analysis of 5 years of satellite observations. *Atmospheric Chemistry and*
954 *Physics*, *10*(4), 1491-1510. doi: 10.5194/acp-10-1491-2010

955 van der Werf, G. R., Randerson, J. T., Giglio, L., van Leeuwen, T. T., Chen, Y.,
956 Rogers, B. M., ... Kasibhatla, P. S. (2017, September). Global fire emissions
957 estimates during 1997–2016. *Earth System Science Data*, *9*(2), 697-720. doi:
958 10.5194/essd-9-697-2017

959 Warneke, C., Bahreini, R., Brioude, J., Brock, C. A., de Gouw, J. A., Fahey, D. W.,
960 ... Veres, P. (2009, January). Biomass burning in Siberia and Kazakhstan as
961 an important source for haze over the Alaskan Arctic in April 2008. *Geophysi-*
962 *cal Research Letters*, *36*(2). doi: 10.1029/2008GL036194

963 Wiedinmyer, C., Akagi, S. K., Yokelson, R. J., Emmons, L. K., Al-Saadi, J. A.,
964 Orlando, J. J., & Soja, A. J. (2011, July). The Fire INventory from
965 NCAR (FINN): a high-resolution global model to estimate the emissions
966 from open burning. *Geoscientific Model Development*, *4*(3), 625-641. doi:
967 10.5194/gmd-4-625-2011

968 Wunch, D., Toon, G. C., Blavier, J.-F. L., Washenfelder, R. A., Notholt, J., Con-
969 nor, B. J., ... Wennberg, P. O. (2011, May). The total carbon column
970 observing network. *Philosophical Transactions of the Royal Society A: Math-*
971 *ematical, Physical and Engineering Sciences*, *369*(1943), 2087-2112. doi:
972 10.1098/rsta.2010.0240

973 Yin, Y., Chevallier, F., Ciais, P., Broquet, G., Fortems-Cheiney, A., Pison, I., &
974 Saunois, M. (2015, December). Decadal trends in global CO emissions as seen
975 by MOPITT. *Atmospheric Chemistry and Physics*, *15*(23), 13433-13451. doi:
976 10.5194/acp-15-13433-2015

977 Yu, K., Keller, C. A., Jacob, D. J., Molod, A. M., Eastham, S. D., & Long, M. S.
978 (2018, January). Errors and improvements in the use of archived meteoro-
979 logical data for chemical transport modeling: an analysis using GEOS-Chem
980 v11-01 driven by GEOS-5 meteorology. *Geoscientific Model Development*,
981 *11*(1), 305-319. doi: 10.5194/gmd-11-305-2018

982 Zhang, Q., Streets, D. G., Carmichael, G. R., He, K. B., Huo, H., Kannari, A., ...
983 Yao, Z. L. (2009, July). Asian emissions in 2006 for the NASA INTEX-
984 B mission. *Atmospheric Chemistry and Physics*, *9*(14), 5131-5153. doi:

985 10.5194/acp-9-5131-2009

986 Zhang, X., Jones, D., Keller, M., Jiang, Z., Bourassa, A. E., Degenstein, D. A., &
987 Clerbaux, C. (2020). Global CO emission estimates inferred from assimilation
988 of MOPITT CO. *Air Pollution Modeling and its Application XXVI*, 219.

989 Zhang, X., Jones, D. B., Keller, M., Walker, T. W., Jiang, Z., Henze, D. K., ...
990 Rochon, Y. (2019, January). Quantifying emissions of CO and NO x using
991 observations from MOPITT, OMI, TES, and OSIRIS. *Journal of Geophysical*
992 *Research: Atmospheres*, *124*(2), 1170-1193. doi: 10.1029/2018jd028670

993 Zheng, B., Chevallier, F., Yin, Y., Ciais, P., Fortems-Cheiney, A., Deeter, M. N., ...
994 Zhao, Y. (2019). Global atmospheric carbon monoxide budget 2000–2017 in-
995 ferred from multi-species atmospheric inversions. *Earth System Science Data*,
996 *11*(3), 1411-1436. doi: 10.5194/essd-11-1411-2019